Sensor selection and miniaturization limits for detection of interictal epileptiform discharges with wearable EEG

Jonathan Dan[1,2], Mette Thrane Foged[3] Benjamin Vandendriessche[2,4], Wim Van Paesschen[5], Alexander Bertrand[2]

[1] KU Leuven, Department of Electrical Engineering (ESAT), STADIUS Center for Dynamical Systems, Signal Processing and Data Analytics, Kasteelpark Arenberg 10, 3001 Leuven, Belgium
[2] Byteflies, Borsbeeksebrug 22, 2600 Berchem, Belgium
[3] Rigshospitalet, Neurobiology Research Unit, 28 Juliane Maries Vej, DK-2100 Copenhagen, Denmark
[4] Department of Electrical, Computer, and Systems Engineering, Case Western Reserve University, Cleveland, OH, United States
[5] UZ Leuven, Department of neurology, Herestraat 49, 3000 Leuven, Belgium

E-mail: jonathan.dan@kuleuven.be

August 2022

Abstract. *Objective* The goal of this paper is to investigate the limits of EEG sensor miniaturization in a set-up consisting of multiple galvanically isolated EEG units to record interictal epileptiform discharges, referred to as 'spikes', in people with epilepsy. *Approach* A dataset of high-density EEG recordings (257 channels) was used to emulate local EEG sensor units with short inter-electrode distances. A computationally efficient sensor selection and interictal spike detection algorithm was developed and used to assess the influence of the inter-electrode distance and the number of such EEG units on spike detection performance. Signal-to-noise ratio, correlation with a clinical-grade IED detector and Cohen's kappa coefficient of agreement were used to quantify performance. Bayesian statistics were used to confirm the statistical significance of the observed results. *Main Results* We found that EEG recording equipment should be specifically designed to measure the small signal power at short inter-electrode distance by providing an input referred noise < 300 nV. We also found that an inter-electrode distance of minimum 5 cm between electrodes in a setup with a minimum of two EEG units is required to obtain near equivalent performance in interictal spike detection to standard EEG. *Significance* These findings provide design guidelines for miniaturizing EEG systems for long term ambulatory monitoring of interictal spikes in epilepsy patients.

Keywords: interictal epileptiform discharge, electroencephalography (EEG), wearable EEG, miniaturization, epilepsy

Submitted to: *J. Neural Eng.*

1. Introduction

Epilepsy is one of the most common severely disabling brain conditions, affecting over 46 million people worldwide [1]. The disorder is characterized by pathological electrical discharges of neurons, which can be recorded non-invasively using scalp electroencephalography (EEG) as isolated spikes or spike-wave complexes. The latter occur during clinical epileptic seizures, but also between seizures (i.e. interictal epileptiform discharges (IED) or 'spikes'), without any concomitant clinical manifestations. EEG is routinely used in the clinic to document such discharges in order to contribute to diagnosis, follow up, and adaptation of treatment for people with epilepsy. Clinical EEG recordings are typically carried out in a hospital (outpatient or inpatient) setting in a resting condition over a relatively short period of time. The American Clinical Neurophysiology Society recommends, that this lasts at least 20 minutes [2]. Therefore, routine EEG often provides only a snapshot of the disorder experienced by a person with epilepsy. Short duration EEG recordings cannot capture long-term patterns of the disorder such as seizure frequency, timing or dynamic cycles [3]. Long-term monitoring of interictal spikes has been shown to be an effective predictor of seizure timing [4] as well as treatment outcome [5]. In order to obtain long-term EEG in realistic conditions, miniaturized EEG devices that can be worn by people in their everyday life would be preferable.

Previous work has demonstrated that EEG recording using several dozens of electrodes, such as those used in clinical routine, are not required to effectively monitor discharge features in people with a diagnosis of epilepsy and that a low number of electrodes can be sufficiently informative [6–9]. Furthermore, wearable EEG devices for everyday life monitoring are in active development [10–14]. Efforts to miniaturize EEG devices have mainly focused either on the electronics of the recording device or on the electrode placement setup. Some examples include the work of Zibrandtsen et al. [14] who made custom fitted in-ear EEG to monitor people with epilepsy. They analyzed intra-ear EEG channels and inter-ear EEG channels and investigated the feasibility of annotating epileptic seizures based on in-ear EEG channels alone. They found ear-EEG can detect temporal lobe seizures and generalized seizures as well as interictal spikes. Swinnen et al. [12] used Byteflies Sensor Dot, a commercial miniature EEG sensor with two channels, to detect typical absence seizures in adults and children. They found epileptologists were able to reliably detect typical absence seizures using this miniature EEG sensor.

One way of further minimizing the EEG setup is by reducing the number of wires. This can be done by using several EEG amplifiers that are each connected to a single pair of electrodes. These isolated EEG sensor units measure a local bipolar channel, each with a built-in local amplifier. Such a set-up with multiple miniaturized and galvanically isolated EEG sensor units eliminates the need for multiple long wires that run across the scalp, and is sometimes referred to as a wireless EEG sensor network [15–17]. The bulkiness of such an EEG sensor network is determined by the number of sensor units and the size of these units. The latter is mostly dependent on the distance between the electrodes of each such sensor unit.

Obviously, reducing the number of recording electrodes increases the importance of electrode placement as it is expected to influence the detection of epileptiform discharges, even for generalized discharges [6]. As a corollary, it is critical to individualize the placement of reduced numbers of electrodes to the specifics of a patient discharge pattern as compared to routine hospital-based recordings.

To approach this electrode placement problem, and to analyze miniaturization effects, a setup with multiple sensor units with short bipolar inter-electrode distances can be emulated and evaluated using information collected through high-density EEG (HD-EEG) recordings. In a 257-electrode HD-EEG head cap, electrodes are situated approximately 2 centimeters apart, thus allowing to emulate short inter-electrode distances. This type of approach has been previously proposed in the context of auditory attention decoding, to identify and quantify the lower bound on miniaturization for EEG-based decoding of neural responses to speech. Mundanad Narayanan et al. showed that for inter-electrode distances equal or greater than 3 cm, the decoding performance was not significantly worse compared to that achieved with long distance channels referenced to the `Cz` electrode [15]. Furthermore, they showed a rapid decline in decoding performance for inter-electrode distances smaller than 3 cm. The study was also performed on an HD-EEG dataset where short distance channels were constructed through re-referencing. Studies on the effect of inter-electrode distance had already been reported in the 1980. Authors showed that the amplitude of the EEG follows an exponential relationship with inter-electrode distance [18]. However, in the context of spike detection, it is not necessarily the decrease in amplitude that impacts the detection performance, but (also) the changes in signal-to-noise ratio as the noise levels will also change with a decrease in inter-electrode distance.

In this paper, we investigate the limits of miniaturization for interictal spike detection using a network of galvanically isolated EEG units by

emulating such a set-up via HD-EEG recorded on people with epilepsy. We present an automated algorithm pipeline for the selection of a small number of EEG channels for mobile EEG ambulatory monitoring and for the automatic detection of inter-ictal epileptiform discharges. The effects of miniaturization, both in terms of short inter-electrode distance and in terms of a small number of EEG units, were assessed through comparison with spike detection on standard 32 channels of 'long-distance' EEG in which all electrodes are wired to a central reference electrode.

Processing of HD-EEG is a computationally heavy operation due to the high number of electrodes resulting in high-dimensional data. In order to study the influence of the number of EEG sensor units and the inter-electrode distance, efficient methods to process these data have to be developed. First a computationally efficient spike detector should be used. Spike events are stereotypical in that spatial and temporal signature of different events are very similar (within the same patient). Algorithms that leverage this build an average spike template that is then used as a matched filter for detecting spikes [19–22]. This type of algorithm is computationally efficient due to the low number of operations required to classify a new epoch of data. In this paper, we use an algorithm that leverages the spatio-temporal signature of spike events by constructing a filter that enhances spikes, but also suppresses non-spike EEG activity and artefacts by exploiting the spatio-temporal second order statistics of the latter components. In this way, the filter maximizes the signal-to-noise ratio (SNR) (i.e. spike to noise ratio) to obtain a more accurate detection than a straightforward matched filter. This filter design paradigm is known as max-SNR filtering [23]. We then select a small number of EEG units using a channel selection procedure to obtain a reduced channel set from a large set of candidate channels. This must also be computationally efficient and should make a selection that is optimized for the spike detection task. In a previous study, we compared different channel selection methods for group-sparse generalized eigenvalue decomposition (GEVD) problems, which is a general class of problems that contains the max-SNR filter as a special case. The group-sparsity appears in the spatio-temporal filter, where selecting one EEG channel corresponds to also selecting all the time lags associated with that channel (representing a group of optimization variables). In the study, we found that for a low number of channels to be selected, a forward greedy selection was the most efficient, while being competitive with more expensive optimization methods [24].

Manual annotation of spike events is a time-consuming activity that requires the expertise of experienced clinical neurophysiologists [25]. It is a difficult task that must meet the six criteria suggested by the International Federation of Clinical Neurophysiology [26]. These criteria define an IED as (1) di- or tri-phasic waves with sharp or spiky morphology (i.e. pointed peak); (2) different wave duration than the ongoing background activity: either shorter or longer; (3) asymmetry of the waveform: a sharply rising ascending phase and a more slowly decaying descending phase, or vice versa; (4) the transient is followed by an associated slow after-wave; (5) the background activity surrounding IED is disrupted by the presence of the IED; and (6) distribution of the negative and positive potentials on the scalp suggests a source of the signal in the brain, corresponding to a radial, oblique, or tangential orientation of the source. While these criteria provide a basis for labeling a spike, inter-rater agreement is only fair, with reported Cohen's kappa coefficient of 0.49 for inter-rater agreement for single spike identification [27], 0.63 for the occurrence of one or more spikes during a 10-second epoch, and 0.69 for a 30-minute epoch [28]. Because of the time required, it is rare for human experts to fully annotate an EEG recording. For diagnostic purposes, the annotation of several clear spike events that allow confirmation of the diagnosis of epilepsy and localization of the seizure onset zone are often sufficient. Human annotation can be facilitated by a spike detection software. Only a few software packages are available on the market with certification for use in clinical practice. Currently, Persyst includes the spike detection algorithm with the highest agreement to human experts [28]. It is a fully automated spike detector based on a deep neural network.

The outline of the paper is as follows. We present the dataset, along with the channel selection and spike detection methodology in section 2. Next, in section 3, we present our results on the effect of inter-electrode distance and number of miniaturized EEG units on the ability to identify spikes. They are discussed and put in perspective with the current corpus of research in section 4. Conclusions and implications of the work are highlighted in section 5.

2. Methods

This section describes the material and methods that were used to conduct the analysis on the limits of EEG sensor miniaturization to record interictal spikes. We first describe the EEG data set in subsection 2.1, after which we describe the different steps of our signal processing methodology in the remaining subsections. The signal processing pipeline consists of the following

steps. First, a base set of annotations for spikes are generated using the automated spike detector provided with the Persyst software. Then, a pool of bipolar channels with a fixed inter-electrode distance is generated by re-referencing the high-density EEG channels. We then propose a spike detector based on a max-SNR filtering criterion. This filter design is then used to perform a data-driven channel selection, where we aim to select the N bipolar channels that maximize the SNR at the output of the filter. A detailed description of each of these steps is presented in the next subsections along with the performance metrics used to evaluate miniaturization limits.

2.1. Recordings

The recordings used in this study were originally obtained between 2015 and 2018 in the context of pre-surgical evaluation of patients with drug-resistant focal epilepsy referred to a tertiary care hospital (Rigshospitalet, Copenhagen, Denmark). HD-EEG recordings were performed over 120 minutes with 257 electrodes with exchangeable sponge electrodes using a EGI Gedodesic Sensor Net HydroCel GSN 130 amplifier and cap sampled at 1 KHz.

2.2. Spike annotations

In order to automate the annotation of IEDs (from hereon referred to as 'spikes'), the recordings were analyzed using Persyst version 14.D software (Persyst Development Corporation, Solana Beach, CA, USA) to annotate the spikes. Persyst is a clinical grade EEG analysis software that specializes in epilepsy diagnosis. It contains a fully automated spike detector based on a deep neural network. To obtain the spike annotations, the software's low-pass and high-pass values were left at their default values (0.16 Hz - 70 Hz). The notch filter was set to 50 Hz. The detection was set to the low sensitivity setting (Persyst score > 0.9), which has high specificity [28]. Spikes occurring during periods contaminated by strong artifacts (peak amplitude $> 200\ \mu V$ or 1 second root-mean-square $> 100\ \mu V$, which are mostly associated with tapping and movement artifacts) and recordings with a low number of spikes such that cross-validation could not be performed (less than 10 spike events) were excluded from the analysis.

2.3. Miniature EEG emulation

The miniaturization analysis was performed by extracting a pool of candidate channels (each representing a separate galvanically isolated EEG sensor unit), with desired inter-electrode distances of either 2, 3.5, 5, 6.5 or 8 cm between electrode pairs (each distance leads to a different pool of candidates which are then standardized across scenarios as explained below). We refer to the inter-electrode distance with the value d. To obtain this pool of bipolar channels, we implemented the following procedure. First, the inter-electrode distance between all possible electrode pairs was computed. The latitude and longitude of each electrode in the EGI Gedodesic Sensor Net HydroCel GSN 130 headset is given by the manufacturer. The distance was computed as the haversine distance with the head modeled as a sphere with a circumference of 57 cm [29]. The haversine distance or great-circle distance is the shortest distance between two points on the surface of a sphere, measured along the surface of the sphere [30]. In the context of EEG sensor units, this distance corresponds to the length of the wire between two electrodes. Figure 2 shows the number of electrode pairs (channels) as a function of the inter-electrode distance. The electrode pairs at a distance $d \pm 0.25$ cm were retained. Since each d results in a different number of candidate channels, a channel selection procedure was then applied to each of the pools in order to obtain an equal number of candidate channels independently of inter-electrode distance d. This selection eliminates redundant channels to obtain a pool of candidate channels that uniformly cover the scalp. Channels were considered redundant with respect to each other if they were geometrically close by and in the same orientation as they would record very similar signals. However, electrode pairs with close midpoints but orthogonal orientation would record relevant information as they record dipoles with different orientations. To this end, we use a proximity metric (p), which combines the distance (d) and the orientation between two channels, based on

$$d = \text{haversine\_distance}(\mathbf{m_1}, \mathbf{m_2}) \tag{1}$$

$$p = e^{(-\frac{2}{3} * d)} * |\mathbf{v_1} \cdot \mathbf{v_2}| \tag{2}$$

where $\mathbf{m_1}, \mathbf{m_2}$ are the midpoints of each channel (i.e. the center point of the great circle line between the two electrodes that define the channel), $\mathbf{v_1}, \mathbf{v_2}$ are the unit orientation vectors of each channel (defining the orientation of the line between the two electrodes that define the channel), and d is the harvesine distance between the midpoints of both channels. The different symbols used in the computation of the proximity metric are illustrated in figure 1. The proximity metric p in equation 2 is computed from the multiplication of the dot product of the two unit orientation vectors and an exponential decay of the distance between the midpoints of both channels. The rate of decay is governed by a constant which reflects the notion of proximity on the scalp. Based on 1-2, the proximity metric is high if the two channels are close to each other (large d), *and* if their orientation is similar (large

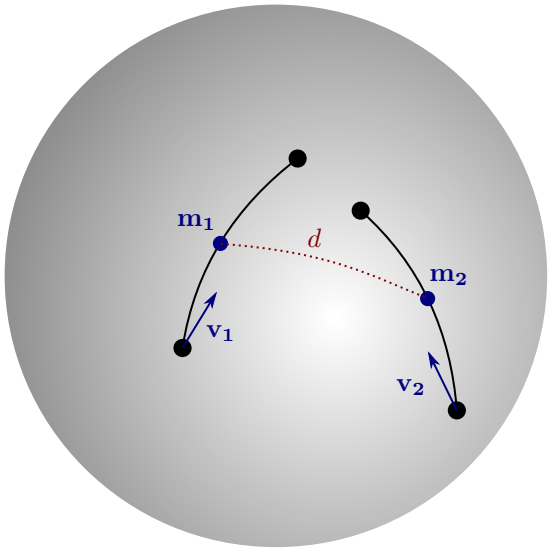

Figure 1: Illustration of the different symbols used in the computation of the proximity between two pairs of electrodes.

$|\mathbf{v_1} \cdot \mathbf{v_2}|$). Indeed, if either the angle between $\mathbf{v_1}$ and $\mathbf{v_2}$ is near-orthogonal or the distance d is large, then p will be small. The local density of a channel was computed as the sum of the proximity p of a channel to all other channels. To obtain a set of 256 channels, the channel with the highest proximity to all other channels was iteratively removed until a set of 256 channels was obtained in each candidate pool.

2.4. Spike detection algorithm

Template matching has been demonstrated to successfully detect neural spiking activity both on intracranial and scalp EEG recordings [19–22].In this paper, we use a filter design framework that is akin to such a template matching filter, with the additional benefit that it takes the noise statistics into account (in this case any non-spike EEG activity) in order to maximize the SNR for the detection. The max-SNR filtering algorithm we use here is a variation of an algorithm we previously developed and validated for the detection of epileptic seizures [8]. It is a pre-trained multi-channel filter, implemented as a filter-and-sum pipeline. The algorithm requires examples of spikes and noise (i.e. non-spike EEG), which are obtained automatically via Persyst executed at a high specificity level (see below).

The raw signals were first downsampled from 1 KHz to 100 Hz, then bandpass filtered between 3 Hz and 30 Hz using a zero-phase, non-causal bandpass filter. The EEG signal in channel k at sample time index t is modeled as

$$x_k(t) = s_k(t) + n_k(t)$$

where $s_k(t)$ corresponds the signal component that contains all the spike events and $n_k(t)$ corresponds to background EEG, which in our case is considered to be noise. The N-channel EEG signal is denoted as $\mathbf{x}(t) \in \mathbb{R}^N$ with $\mathbf{x}(t) = [x_1(t) \ \ldots \ x_N(t)]$. The aim is to produce a filter $\mathbf{w} \in \mathbb{R}^N$ that filters and combines the N channels of EEG into a single-channel output signal $o(t)$ in which the background EEG is maximally suppressed, while preserving the spikes. This output channel is obtained through the linear combination:

$$o(t) = \mathbf{w}^T \mathbf{x}(t) \tag{3}$$

From a signal processing viewpoint, $\mathbf{w}$ acts as a spatial filter that linearly combines different EEG channels at different positions on the scalp. The filter $\mathbf{w}$ is optimized in a data-driven fashion to maximize the SNR of $o(t)$ over a training set, i.e. solving

$$\max_{\mathbf{w}} \frac{E\{(\mathbf{w}^T \mathbf{s}(t))^2\}}{E\{(\mathbf{w}^T (\mathbf{n}(t))^2\}} = \max_{\mathbf{w}} \frac{\mathbf{w}^T \mathbf{R_s} \mathbf{w}}{\mathbf{w}^T \mathbf{R_n} \mathbf{w}} \tag{4}$$

where $E\{.\}$ denotes the expected value operator, $\mathbf{R_s} = E\{\mathbf{s}(t)\mathbf{s}(t)^T\}$ and $\mathbf{R_n} = E\{\mathbf{n}(t)\mathbf{n}(t)^T\}$ denote the spike and noise covariance matrices, respectively, and $\mathbf{s}(t)$ and $\mathbf{n}(t)$ are defined similarly to $\mathbf{x}(t)$, i.e., $\mathbf{x}(t) = \mathbf{s}(t) + \mathbf{n}(t)$. In subsection 2.4.1, we will explain how these covariance matrices $\mathbf{R_s}$ and $\mathbf{R_n}$ are estimated from the data. It can be shown [23] that the solution of the maximization problem defined in equation 4 is the eigenvector corresponding to the largest eigenvalue of the matrix $\mathbf{R_n^{-1}} \mathbf{R_s}$. This is equivalent to solving a generalized eigenvalue decomposition (GEVD) problem based on the matrix pencil $(\mathbf{R_s}, \mathbf{R_n})$ [23].

The filter described above is a spatial filter. It can be expanded to a causal spatio-temporal filter by creating a buffer of L samples for each channel and stacking all buffered (time-lagged) samples in a single vector $\tilde{\mathbf{x}}(t) = col\{\tilde{\mathbf{x}}_\mathbf{1}(t), \ldots, \tilde{\mathbf{x}}_\mathbf{N}(t)\}$ where $\tilde{\mathbf{x}}_\mathbf{k}(t) = [x_k(t), x_k(t-1), \ldots, x_k(t-L+1)]^T$ and $col\{.\}$ denotes a columnwise stacking. The output signal $o(t)$ is given by equation 3 where $\mathbf{w}$ is replaced by $\tilde{\mathbf{w}} \in \mathbb{R}^{LN}$ and $\mathbf{x}(t)$ is replaced by $\tilde{\mathbf{x}}(t) \in \mathbb{R}^{LN}$. This then corresponds to a filter-and-sum operation, where each channel is filtered with a channel-specific finite impulse response filter of length L, followed by a summation across channels. For spike detection the buffer length is set to 200 ms ($L = 20$ at 100 Hz sampling), corresponding to the full duration of a spike discharge.

In this spatio-temporal extension, the covariance matrices in equation 4 are replaced with their spatio-temporal generalizations, i.e., $\mathbf{R_s} = E_s\{\tilde{\mathbf{s}}(t)\tilde{\mathbf{s}}(t)^T\}$ and $\mathbf{R_n} = E_i\{(\tilde{\mathbf{n}}(t))(\tilde{\mathbf{n}}(t))^T\}$. In the remainder of the paper, we always assume the spatio-temporal extension unless otherwise specified, and omit the $\tilde{}$ for notational convenience.

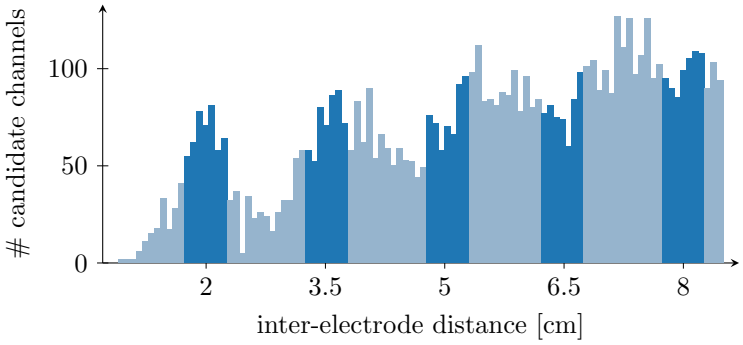

Figure 2: Histogram of the inter-electrode distance between all electrodes in a EGI Geodesic Sensor Net HydroCel GSN 130 headset with 257 electrodes. Distances of 2, 3.5, 5, 6.5 and 8 cm ±0.25 cm, highlighted in darker blue, are investigated in this study.

2.4.1. Covariance matrix estimation In order to compute the optimal filter $\mathbf{w}$, we need to estimate the two covariance matrices $\mathbf{R_s}$ and $\mathbf{R_n}$ on a training data set.

In our implementation of the algorithm, the spike covariance matrix $\mathbf{R_s}$ is estimated based on a training set $\mathcal{S}$ with a few example ‡ spike waveforms of the patient under test. To this end, we used the following estimator § ‖

$$\mathbf{R_s} \approx \frac{1}{L|\mathcal{S}|} \sum_{\tau \in \mathcal{S}} f(\tau) \sum_{t=\tau}^{\tau+L} \mathbf{x}(t)\mathbf{x}(t)^T \tag{5}$$

$$f(\tau) = g\left(\sum_{t=\tau}^{\tau+L} ||\mathbf{x}(t)^2||_1 \left(\frac{\sum_{\nu \in \mathcal{S}} \sum_{t=\nu}^{\nu+L} ||\mathbf{x}(t)^2||_1}{|\mathcal{S}|} \right)^{-1} \right) \tag{6}$$

$$g(x) = \begin{cases} 1 & \text{if } x < 1 \\ \frac{1}{x} & \text{if } x >= 1 \end{cases} \tag{7}$$

where $\mathcal{S}$ is the set of time indices corresponding to the first time sample of each 'spike' segment marked by the Persyst spike detector. $f(\tau)$ is a normalization of the power of a spike event with respect to the average power of all spike events for events with above-average power. It is used to reduce the influence of outlier spikes with high power (i.e., above-average). The noise covariance matrix $\mathbf{R_n}$ was computed similarly without the normalization factor as

$$\mathbf{R_n} \approx \frac{1}{|\mathcal{N}|} \sum_{t \in \mathcal{N}} \mathbf{x}(t)\mathbf{x}(t)^T$$

where $\mathcal{N}$ is a set of training samples that do not contain a spike event. Since most of the data does not contain spikes (as IEDs are sparse events), it is not a problem if some spikes leak into $\mathbf{R_n}$, as they will not have a large impact in the overall sum.

2.4.2. Regularization The inclusion of time lags substantially increases the dimension of the covariance matrices, possibly making them ill-conditioned due to redundancy in the entries of $\mathbf{x}(t)$. For this reason a regularization scheme is required. Wouters et al. [31] proposed an effective regularization scheme for a template-matching-filter that optimizes a similar cost function as in equation 4, but where the numerator consists of a single template instead of a covariance matrix. The regularization is obtained by projecting the data on a subspace containing the main principal components of the denominator covariance matrix along with the template itself (to represent the target signal). In this work we adapted the method to our problem formulation. The data were projected on a subspace defined as the span of the principal components of both the noise $\mathbf{R_n}$ and spikes $\mathbf{R_s}$ covariance matrices. The principal components with the largest eigenvalues of $\mathbf{R_n}$ and accounting for 85% of the variance in the noise segments were retained. The principal components with the largest eigenvalues of $\mathbf{R_s}$ accounting for 95% of the variance in the spike segments were also retained. These two sets of principal component vectors were then combined and orthogonalized by placing them in the

‡ These examples can be obtained, e.g., from a manual annotation on part of the data, or via automatic annotation with clinical-grade software such as Persyst in high-specificity modus to extract a few examples with a minimal number of false positives.

§ It is noted that the estimator (5) does not contain the mean subtraction that is usually present in the definition of a covariance matrix. This is because $\mathbf{R_s}$ as it is defined in (4) does not have this mean subtraction, since the filter design should take a mean offset in the signals into account. However, since our data is high-pass filtered, the signals are zero-mean in the long term.

‖ Note that, since the noise floor is always present, the resulting covariance matrix is actually an estimate for $E\{(\mathbf{s}(t)+\mathbf{n}(t))(\mathbf{s}(t)+\mathbf{n}(t))^T\} = \mathbf{R_s} + \mathbf{R_n}$. However, since replacing $\mathbf{R_s}$ with $(\mathbf{R_s} + \mathbf{R_n})$ in (4) leads to the equivalent optimization problem $\max_{\mathbf{w}} 1 + \frac{\mathbf{w}^T\mathbf{R_s}\mathbf{w}}{\mathbf{w}^T\mathbf{R_n}\mathbf{w}}$, we obtain the same optimal filter.

columns of a new matrix $\mathbf{M}$ on which a singular value decomposition is applied to find an orthogonal basis for the subspace. Let $\mathbf{U} = [\mathbf{u}_1 \dots \mathbf{u}_K]$ denote the matrix, the columns of which consist of the K left singular vectors corresponding to the largest singular values of $\mathbf{M}$, where the cut-off K is chosen such that the cumulated sum of these singular values is at least 99% of the sum of all singular values. The matrix $\mathbf{U}$ is then used as a compression matrix on the data, i.e.

$$\mathbf{x_c}(t) = \mathbf{U}^T\mathbf{x}(t)$$

where $\mathbf{x_c}(t) \in \mathbb{R}^K$. The optimal compressed filter $\mathbf{w_c}$ is then given as the eigenvector of $(\mathbf{R}_{\mathbf{n,c}}^{-\mathbf{1}})\mathbf{R}_{\mathbf{s,c}}$, where $\mathbf{R_{n,c}} = \mathbf{U}^T\mathbf{R_n}\mathbf{U}$ and $\mathbf{R_{s,c}} = \mathbf{U}^T\mathbf{R_s}\mathbf{U}$ correspond to the compressed matrices. The filter output is then defined as $o(t) = \mathbf{w_c}^T\mathbf{x_c}(t)$ which is equivalent to an uncompressed filtering $o(t) = \mathbf{w}^T\mathbf{x}(t)$ with $\mathbf{w} = \mathbf{U}\mathbf{w_c}$. It is noted that this compression is only applied with the purpose of regularization during training to obtain a better (uncompressed) filter $\mathbf{w}$. During operation of the algorithm (at test time), we always apply the full filter $\mathbf{w}$ on the uncompressed data, as the compression with $\mathbf{U}$ requires more computations than the filtering with $\mathbf{w}$.

2.4.3. Classification The classification of an epoch as containing spikes was performed twice per second (i.e. at 0.5 Hz). As the filter is trained to suppress non-spike EEG and enhance spikes, we can perform detection based on the output power or root mean square (RMS) value of the filter. Therefore, as features for the classifier, we used the moving average root mean square (RMS) value of the single-channel filter output $o(t)$ averaged over 200 ms (i.e. the duration of a spike) and the moving average RMS averaged across the different channels of the EEG data $\mathbf{x}(t)$ and averaged over one second (the latter serves as a baseline reference). The downsampling to 0.5 Hz was done with a bucket algorithm [32]. This algorithm preserves the amplitude of short duration local extrema such as spikes that would otherwise be attenuated by a standard low-pass and decimation algorithm. These two RMS features were log transformed before being fitted by a linear discriminant analysis (LDA) classifier, which was trained based on the spike annotations in the training set.

2.5. Greedy Forward Channel selection

To reduce the number of channels from 256 candidates, a channel selection procedure is required. As we are assessing the performance of a spike detection task based on a max-SNR framework, which is equivalent to solving a GEVD problem [23], the channel selection task corresponds to a (group)-sparse GEVD problem. In Dan et al. [24] the performance of various group-sparse variable selection methods for GEVD problems has been investigated. It was found that greedy forward selection performed competitively with other state-of-the-art methods at a significantly lower computational cost. In the present study, where the number of input channels is high, it is necessary to use a channel selection method with a tractable computational complexity, which is why we indeed adopt a forward greedy selection. The forward selection method starts from an empty set of channels $\mathcal{C}$ and sequentially adds the channel that maximally increases the objective in equation 4 when added to the current set $\mathcal{C}$. New channels are added until $\mathcal{C}$ contains M channels, where M is a pre-defined number of required channels. Some examples of selected channels are shown in figure 3.

2.6. Training scheme

Training and testing was performed individually for each subject. When evaluating the effect of inter-electrode distance, care was taken to separate the dataset in independent training and testing sets. The spike epochs were split in four folds of equal size. The rest of the non-spike data were also split in four folds each containing 30 minutes of data. Each training fold used three folds of spike epochs and three folds of non-spike data in order to estimate the covariance matrices $\mathbf{R_s}$ and $\mathbf{R_n}$. The obtained filter w defined in equation 4 was then evaluated on the remaining spike fold and remaining non-spike fold. This process was repeated four times.

2.7. Evaluation metrics

Since the real ground truth is unknown, we propose several indirect metrics to assess the quality of the spike detections.

2.7.1. Signal-to-Noise Ratio The average spike signal power over 200 ms was computed as the average RMS amplitude over all channels in all segments that were flagged as spikes by Persyst (note that we used Persyst in the high specificity setting, such that the effect of the false positive detections are assumed to be negligible). The noise power was computed in a similar fashion over all non-spike segments. The ratio of both RMS values was then used as the SNR metric.

2.7.2. Correlation To compare the Persyst detections and the detections of our max-SNR pipeline, a correlation score was computed for each subject between the average spike events detected by both algorithms. The correlation score allows to compare the morphology of the detected spike waveforms of

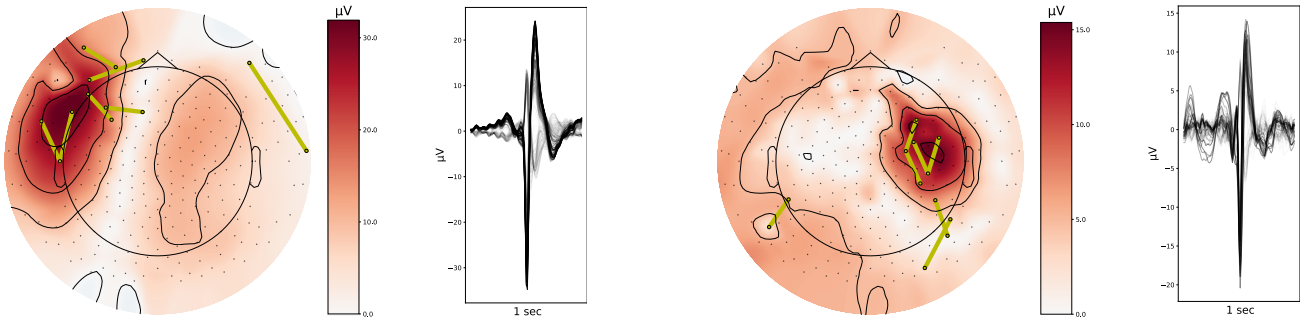

Figure 3: Example of seven channels selected in two example subjects. The inter-electrode distance of the channels is set to 5 cm. The topoplot shows the magnitude of the average spike of Persyst at the peak of the spike (t=0) in a common average montage. The 1 second timecourse of the average spike is shown with all channels superimposed. The figure illustrates the automatic channel selection results. Maximising the signal to noise ratio results in a selection with most channels close to the electrodes with highest peak magnitude. Note that some channels far away from the spike with possibly little correlation to the spike activity are selected which allows the algorithm to cancel some of the noise components.

both algorithms. A high correlation indicates that the number of false positive detections of the max-SNR filter is small (as these would have a distorting effect on the waveform). Indeed, since Persyst is used in the low sensitivity mode [28] (resulting in a high specificity, i.e., very few false positives), the average waveform of both approaches should be similar. The events were first aligned to the maximum of the absolute value over a 0.5 second epoch across all channels. The average 0.5 second event was then constructed. The Pearson-correlation coefficient was computed per channel between the average of the spikes detected by Persyst and the spikes annotated by the max-SNR pipeline. The average correlation coefficient was computed as the weighted sum over all channels where the weight was given by the power of the channel in the Persyst average spike event.

2.7.3. Agreement score Cohen's kappa coefficient of agreement was used as the agreement score. It was computed between the baseline performance of the max-SNR detection pipeline when trained with 32 channels referenced to `Cz` and between the different short inter-electrode distance scenarios. The inter-rater agreement between humans in annotating IEDs reaches a Cohen's kappa of 0.49 for detecting individual spikes [27]. We therefore consider a kappa larger than 0.5 to be in the region of practical equivalence (ROPE).

2.8. Statistical analysis

A Bayesian analysis was performed to evaluate the probability of obtaining a Cohen's kappa coefficient > 0.5 for the different short distance scenarios (when comparing with the baseline). This is the level of agreement obtained between human experts annotating interictal spikes [27]. The analysis was based on the generation of a large number of samples from distributions that fit to the observed data. A Bayesian analysis allows to estimate the probability of observing a parameter based on observed measurements and a prior assumption on the underlying distribution of the parameter. The observed Cohen's kappa was modeled as a $\mathcal{B}$-distribution as is appropriate for a variable bound to [0, 1] [33]. The $\mathcal{B}$-distribution was expressed in terms of mean and variance as was proposed in [34]. The mean and variance are set by a prior distribution with fixed parameters and are used to generate different distributions of Cohen's kappa coefficient. As proposed in [35], the means were drawn from a $\mathcal{B}$-distribution whose mean and variance was set to the mean and variance of Cohen's kappa coefficients in the full data set (i.e. across different subjects, folds, inter-electrode distances, and number of EEG units).. The variance was drawn from a uniform distribution in the interval between 0 and two times the variance of the whole data. The model is represented schematically in figure 4. PyMC 4.1.4 [36] was used to generate the model.

The complete code for the simulations is provided online : `https://github.com/danjjl/miniEEG`

3. Results

3.1. Recordings

A total of 40 subjects were processed by Persyst for spike annotations. Fifteen subjects had ten or more spike events meeting the inclusion criteria and were included in the analysis. A total of 4088 spikes were detected by Persyst. The median number of spikes per subject was 58 (range 27-1190) The number of spike events detected by Persyst are given per subject in

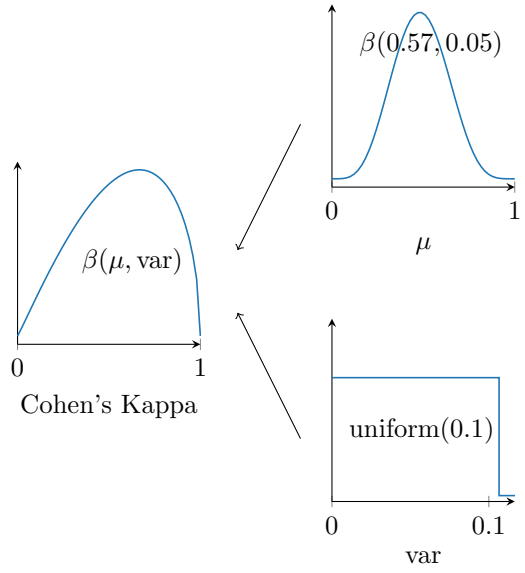

Figure 4: Schematic representation of the Bayesian model. Cohen's kappa coefficient is modeled as a β distribution with parameters obtained from a β distribution for the mean (μ) and a uniform distribution for the variance (var).

	# spikes
subject 1	1190
subject 2	1016
subject 3	439
subject 4	401
subject 5	375
subject 6	231
subject 7	111
subject 8	58
subject 9	47
subject 10	45
subject 11	43
subject 12	40
subject 13	38
subject 14	27
subject 15	27
Total	4088

Table 1: Number of interictal epileptiform discharges detected by Persyst 14 at the low sensitivity setting.

table 1.

3.2. Signal power

The power of the spike events annotated by Persyst is reported as a function of inter-electrode distance. The power is reported as an average across channels for the channels selected by the channel selection algorithm when 1-10 channels are selected. Figure 5.a shows that the median spike RMS at an inter-electrode distance of 2 cm is 4 μV and increases to 12 μV at 8 cm. The SNR is shown as a function of distance in 5.b. As opposed to the spike RMS, It shows a near equal SNR independent of distance with a median SNR of 1.4 at 2 cm and 1.5 at 8 cm. This implies that both the power of the spikes as well as the background noise are reduced by an equal amount when reducing the inter-electrode distances.

3.3. Correlation between Persyst and the max-SNR pipeline

In order to validate our computationally efficient max-SNR based spike detection pipeline, we compared the spikes detected by Persyst to the spikes detected by the max-SNR based detection pipeline when electrodes were referenced to `Cz` and 32 channels were selected using the automatic channel selection algorithm. Both algorithms detect events such that the average spike waveform of both algorithms have a very high correlation. The distribution of average spike correlations is given in figure 6.b. It shows a median correlation of 0.94. An example of the average spike of both algorithms for subject 15 is given in 6.a. The number of events detected by the max-SNR algorithm is four times higher than the number of events Persyst detected at the low sensitivity setting. In total, across all subjects, the max-SNR algorithm detected 16937 events while Persyst detected 4088.

3.4. Cohen's kappa coefficient as a function of number of EEG units and distance

Cohen's kappa coefficient of agreement is computed between the max-SNR spike detections on 32 channels referenced to `Cz` and max-SNR spike detections when the number of channels was restricted between one and ten and the inter-electrode distance was fixed to 2, 3.5, 5, 6.5, 8 cm. A boxplot of these different comparisons is shown in figure 7. The median of Cohen's kappa coefficient increases both with the number of units and with the inter-electrode distance. For an inter-electrode distance of 2 cm, the median coefficient is always below 0.5 for three or less nodes. From 3.5 cm, it increases above 0.5 for two or more EEG units.

The Bayesian framework is used to test the confidence of these findings. All simulated MCMC reported convergence with the Gelman-Rubin statistic equal to one for all variables. The probability of the mean Cohen's kappa coefficient being greater than 0.5 is reported in figure 8. It shows a probability $< 95\%$ when using a single EEG unit. It shows a probability $> 95\%$ when using seven or more EEG units at distances of 2 and 3.5 cm. It shows a probability $> 95\%$ when using two or more EEG units at distances of 5 cm or more.

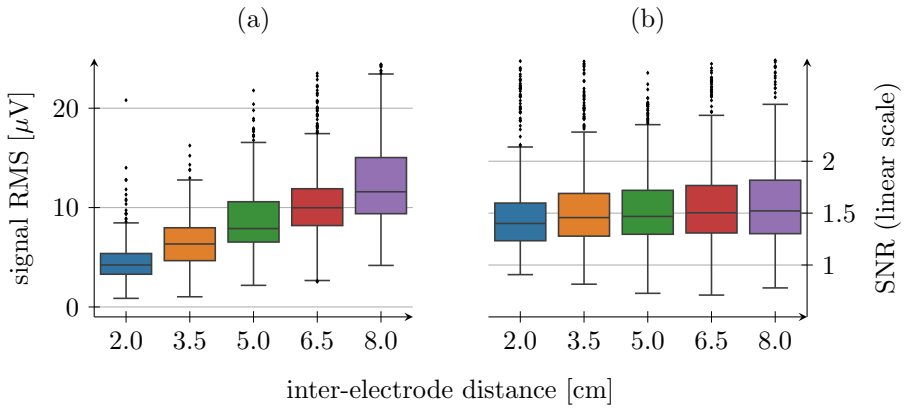

Figure 5: Boxplots of (a) spike root-mean-square (RMS) amplitude as a function of distance and (b) spike RMS to noise RMS ratio as a function of distance over 15 subjects and 1-10 EEG channels.

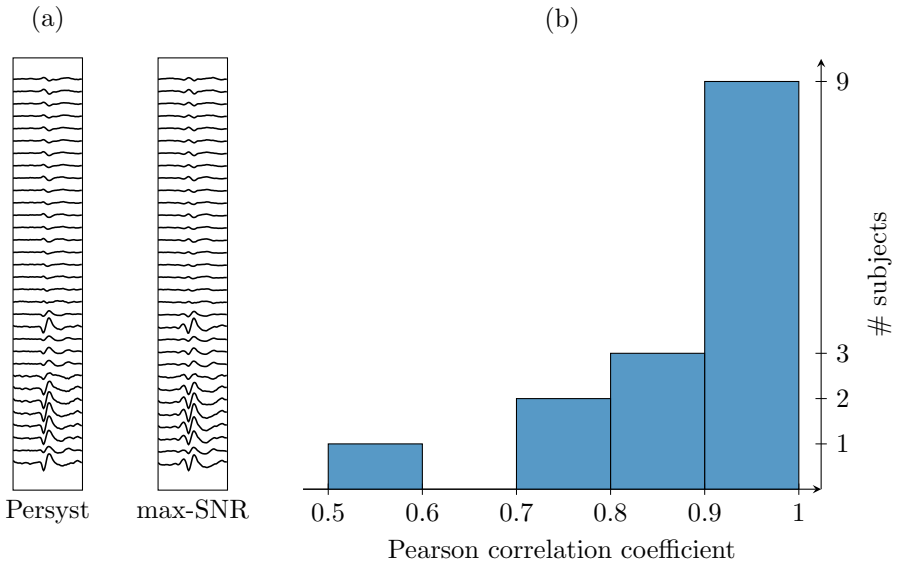

Figure 6: Comparison of the average spike event from patient 15 detected by Persyst and by the max-SNR pipeline. (a) Example average spike event : (left) Persyst, (right) max-SNR pipeline. One second of data is shown with 32 electrodes referenced to `Cz`. (b) Histogram across all patients of the Pearson correlation between the average spike event of both algorithms.

4. Discussion

In this paper, we investigated the effect of inter-electrode distance and influence of the number EEG channels on the ability to record and detect spikes using a set of galvanically isolated miniature EEG sensor units. We analyzed data recorded for clinical purposes with a 257 electrode HD-EEG setup. We annotated the data for spikes using the Persyst 14.D tool, which has been widely utilized in clinical practice and research for seizure and spike detection on EEG. We then measured the RMS amplitude of the detected spikes after re-referencing to short inter-electrode distances. We found that the median RMS of spike events measured with an inter-electrode distance of 2 cm was 4 μV (see figure 6.A). This is about three times lower signal power than found at greater electrode distances and results in signals that are close to the noise floor of standard EEG equipment. In standard clinical care, the American Clinical Neurophysiology Society states that EEG recording devices should add less than 1 μV peak-to-peak noise at any frequency in the band [0.5 - 100] Hz [37]. This is in line with amplifier technology commonly found in EEG equipment, such as the Texas Instrument ADS1299 which claims an input referred-noise of 1 μV peak-to-peak [38]. This indicates that EEG devices with short inter-electrode distances should aim for lower input referred noise.

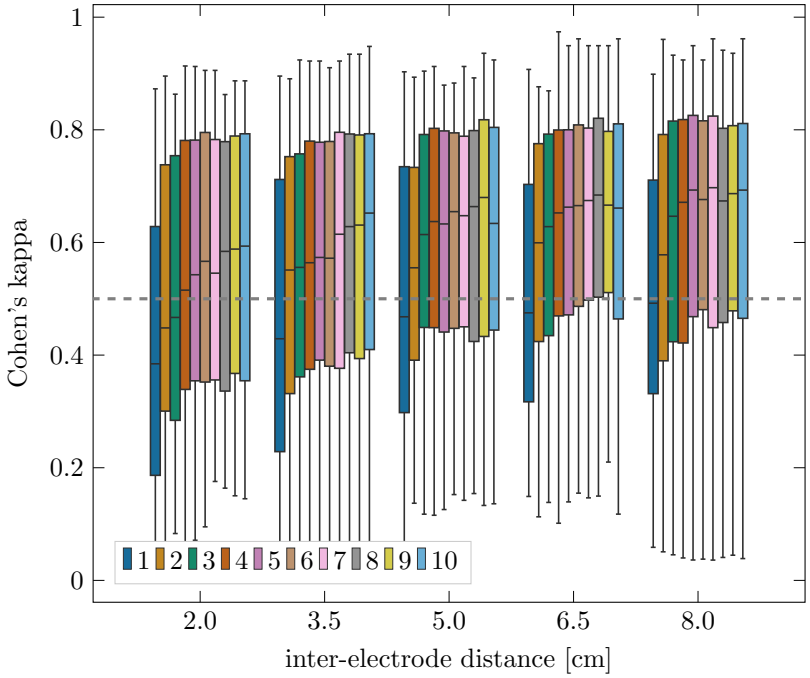

Figure 7: Boxplot of Cohen's kappa coefficient of agreement of detected spike events between the different test scenarios (varying distance and number of channels) using a max-SNR pipeline and a reference max-SNR pipeline on 32 channels referenced to `Cz`. The different colors represent different number of EEG units. The dashed grey line shows the agreement between human raters.

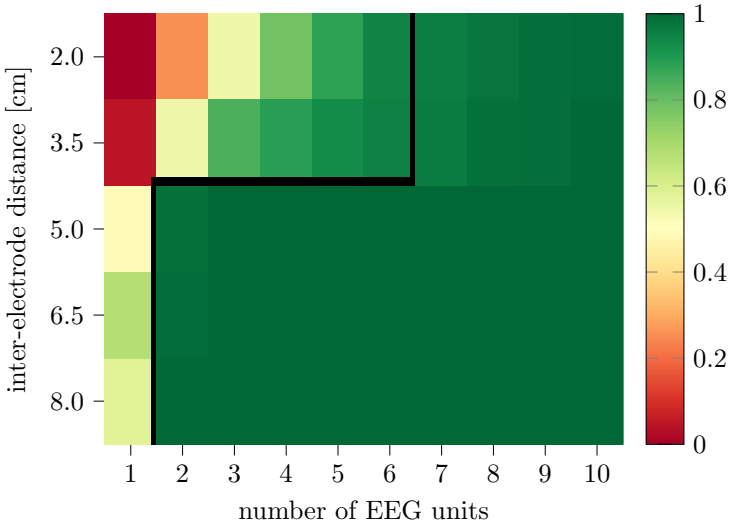

Figure 8: Probability in a Bayesian model of observing a mean Cohen's kappa coefficient of agreement > 0.5 between spike events detected in different test scenarios (varying distance and number of EEG units) using a max-SNR pipeline and a reference max-SNR pipeline on 32 channels referenced to `Cz`. The black line shows the 95% probability boundary.

This is a similar observation as in [39]. Our findings suggest that devices aiming for 2 cm inter-electrode distance should be designed for an input referred noise < 300 nV (three times lower than current standard as suggested by spike amplitude). We also compared the spike RMS to the non-spike RMS (SNR) as a function of inter-electrode distance. This SNR results both from physiological processes as well as extra-physiological such as electronic noise. We found a ratio of 150%. This is in line with the definition of spikes, which state

that spikes should stand out from the background EEG activity [26]. The SNR was only minimally impacted by the inter-electrode distance with the SNR at 140% for an inter-electrode distance of 2 cm. This indicates that spike activity is still distinguishable at 2 cm with scalp EEG. This also means that the amplitude of the spikes and the noise (i.e. background non-spike EEG) is reduced with a similar factor. A similar observation was also made in [39] for the case of event-related potentials.

We compared the spike annotations from the Persyst software on the original 257 electrodes to the annotations using our channel selection and detection pipeline constrained to 32 channels referenced to `Cz`. We found that Persyst detected about four times less spikes than our proposed algorithm. However, we observed a median Pearson correlation of 0.94 between the average spike event detected by both algorithms, with a single subject with a correlation of less than 0.77. For this subject, Persyst does not detect a clear spike pattern. The maximum amplitude of the average spike is 9 μV with no clear spike morphology. The high median correlation indicates a very good agreement on the morphology of spikes between both algorithms and is a point of validation to demonstrate that our algorithm does detect valid spike events. This indicates that the additional spikes detected by the max-SNR filter are actual spikes instead of false positives, implying that Persyst misses a large fraction of the spike events. The latter is expected, since we set Persyst to low sensitivity mode because this is the mode with the highest specificity. In this setting, Reus et al. observed a specificity of 99% when compared to human experts [28]. This setting allows us to use Persyst as reliable ground truth data to accurately estimate the $\mathbf{R_s}$ covariance matrix with minimal leakage of non-spike events in the estimation of $\mathbf{R_s}$.

We compared the spike annotations between a baseline version of our detection pipeline referenced to `Cz` in a 32 channel setting with the annotations from our pipeline constrained to short inter-electrode distances and less than ten channels. We used the Bayesian estimation framework [35] to estimate the probability of obtaining high agreement. This Bayesian testing confirmed a probability $> 95\%$ of obtaining an agreement > 0.5 for inter-electrode distances greater than 5 cm when using two or more EEG units (which corresponds to an agreement that is at least as good as an inter-rater agreement of human annotators, for which Cohen's kappa is 0.49 [27]). In general, we found an influence of both the distance and the number of EEG units on Cohen's kappa coefficient of agreement, while increasing distance increases agreement. Increasing the number of EEG units also increases agreement. In particular going from a single to two (or more) EEG units results in a major increase in the kappa coefficient. From figure 7 and figure 4, we can also observe the interaction between the inter-electrode distance and the number of nodes. It is observed that the influence of the number of EEG units is stronger at small inter-electrode distances (i.e. between 2 and 3.5 cm). For such short distances, there is a clear added value when increasing the number of EEG units. For distances of 5 cm or higher, good performance is obtained with merely 3 EEG units, and there is not much to gain anymore when we increase the number of EEG units. For the shortest distance (2 cm), at least 4 EEG units are required to obtain a median performance that exceeds the agreement of human raters, whereas 2 EEG units are enough to reach this agreement level if the inter-electrode distance is 3.5 cm or higher. These findings indicate that a network of galvanically isolated short distance EEG units is an appropriate setup to monitor spikes and is comparable to a 32 channel setup referenced to `Cz`. It also shows that carefully placed units and increasing the number of units can counteract the decrease in performance obtained by shortening the inter-electrode distance.

Current efforts to miniaturize EEG systems are not limited to the field of epilepsy. In the hearing aid community, several research groups have investigated miniaturization of EEG systems to integrate them with hearing aids. In a recent study, Mundanad Narayanan et al. showed that for inter-electrode distances equal or greater to 3 cm, the decoding of neural responses to speech was not significantly worse to that achieved with long distance channels referenced to the `Cz` electrode [15] when using an appropriate number of EEG units. While a direct comparison to a spike detection task is impossible, given the differences in the nature of the neural response localization and amplitude, both our study and the studies in the hearing aid community show networks of galvanically isolated short distance EEG units are able to capture an EEG signal of interest.

The design objective of short distance EEG units is to allow for measurement of EEG in real-life conditions. This study was conducted on data acquired in a hospital setting. Recordings obtained in uncontrolled conditions during everyday life are expected to contain more artifacts than measured in the controlled setting of the epilepsy monitoring unit. Therefore, reproducibility of the findings we report on a minimal number of channels and inter-electrode distance should now be tested in everyday life activity conditions. When designing an ambulatory setup, robustness should be considered. This could be done by increasing the number of channels and/or inter-

electrode distance above our minimal requirements findings. Improvements to the spike detection algorithm could also be made for example by building a filter that discriminates between epileptic spikes and non-epileptic peak interferers as was suggested in [8].

5. Conclusion

We found that EEG recording equipment should be specifically designed to measure the small signal power at short inter-electrode distance by providing an input referred noise $<$ 300 nV. We also found an inter-electrode distance of 5 cm between electrodes in a setup with a minimum of two EEG units is required to obtain near equivalent performance in interictal spike detection to standard EEG. These findings provide design guidelines for EEG equipment miniaturization in the context of detection of interictal epileptic discharges.

6. Acknowledgements

We thank Michael Guess from Persyst (Solana Beach, CA, USA) and Astrid Devulder (UZ Leuven, Belgium) for their help in configuring and running the Persyst analyis. We also thank Olaf B. Paulson, Lars Pinborg, Sándor Beniczky and the Neurobiology Research Unit of Rigshospitalet (Copenhagen, Denmark) for their thorough work in collecting, documenting and sharing the HD-EEG dataset.

This work was supported by VLAIO and Byteflies through a Baekeland grant (HBC.2018.0189), FWO project nr. G0A4918N, the European Research Council (ERC) under the European Union's Horizon 2020 Research and Innovation Programme (grant agreement No 802895), and the Flemish Government (AI Research Program).

References

1. Beghi, E. *et al.* Global, regional, and national burden of epilepsy, 1990–2016: a systematic analysis for the Global Burden of Disease Study 2016. *The Lancet Neurology* **18,** 357–375 (2019).
2. Sinha, S. *et al.* American Clinical Neurophysiology Society Guideline 1: Minimum Technical Requirements for Performing Clinical Electroencephalography. *Journal of clinical neurophysiology* **33,** 303–307 (4 2016).
3. Baud, M. O. *et al.* Multi-day rhythms modulate seizure risk in epilepsy. *Nature Communications* **9,** 1–10 (1 2018).
4. Karoly, P. J. *et al.* Interictal spikes and epileptic seizures: their relationship and underlying rhythmicity. *Brain* **139,** 1066–1078 (4 2016).
5. Krendl, R., Lurger, S. & Baumgartner, C. Absolute spike frequency predicts surgical outcome in TLE with unilateral hippocampal atrophy. *Neurology* **71,** 413–418 (6 Aug. 2008).
6. Duun-Henriksen, J. *et al.* Channel selection for automatic seizure detection. *Clinical Neurophysiology* **123,** 84–92 (1 2012).
7. Vandecasteele, K. *et al.* Visual seizure annotation and automated seizure detection using behind-the-ear electroencephalographic channels. *Epilepsia* **61,** 766–775 (4 2020).
8. Dan, J., Vandendriessche, B., Paesschen, W. V., Weckhuysen, D. & Bertrand, A. Computationally-Efficient Algorithm for Real-Time Absence Seizure Detection in Wearable Electroencephalography. *International Journal of Neural Systems* **30** (11 2020).
9. Tacke, M. *et al.* Effects of a reduction of the number of electrodes in the EEG montage on the number of identified seizure patterns. *Scientific Reports* **12,** 1–7 (1 Mar. 2022).
10. Casson, A. J. Wearable EEG and beyond. *Biomedical Engineering Letters* **9,** 53–71 (1 2019).
11. Valentin, O. *et al.* Custom-Fitted In- and Around-the-Ear Sensors for Unobtrusive and On-the-Go EEG Acquisitions: Development and Validation. *Sensors* **21,** 2953 (9 2021).
12. Swinnen, L. *et al.* Accurate detection of typical absence seizures in adults and children using a two-channel electroencephalographic wearable behind the ears. *Epilepsia* **62,** 2741–2752 (11 2021).
13. Frankel, M. A. *et al.* Wearable Reduced-Channel EEG System for Remote Seizure Monitoring. *Frontiers in Neurology* **12,** 1842 (2021).
14. Zibrandtsen, I. C., Kidmose, P., Christensen, C. B. & Kjaer, T. W. Ear-EEG detects ictal and interictal abnormalities in focal and generalized epilepsy – A comparison with scalp EEG monitoring. *Clinical Neurophysiology* **128,** 2454–2461 (12 2017).
15. Narayanan, A. M., Zink, R. & Bertrand, A. EEG miniaturization limits for stimulus decoding with EEG sensor networks. *Journal of Neural Engineering* **18,** 056042 (5 2021).
16. Baijot, M. *et al. A miniature EEG node for synchronized wireless EEG sensor networks* in (MDPI, 2021).
17. Bertrand, A. Distributed Signal Processing for Wireless EEG Sensor Networks. *IEEE Transactions on Neural Systems and Rehabilitation Engineering* **23,** 923–935 (6 2015).

18. Epstein, C. M. & Brickley, G. P. Interelectrode distance and amplitude of the scalp EEG. *Electroencephalography and Clinical Neurophysiology* **60,** 287–292 (4 Apr. 1985).
19. Quon, R. *et al.* AiED: Artificial intelligence for the detection of intracranial interictal epileptiform discharges. *Clinical neurophysiology* **133,** 1–8 (2022).
20. Jin, J., Dauwels, J., Cash, S. & Westover, M. SpikeGUI: software for rapid interictal discharge annotation via template matching and online machine learning. *Annual International Conference of the IEEE Engineering in Medicine and Biology Society* **2014,** 4435–4438 (2014).
21. Jing, J. *et al.* Rapid annotation of interictal epileptiform discharges via template matching under Dynamic Time Warping. *Journal of neuroscience methods* **274,** 179–190 (2016).
22. Lodder, S., Askamp, J. & van Putten, M. Interictal spike detection using a database of smart templates. *Clinical neurophysiology* **124,** 2328–2335 (12 2013).
23. Veen, B. D. V. & Buckley, K. M. Beamforming: A Versatile Approach to Spatial Filtering. *IEEE ASSP Magazine* **5,** 4–24 (2 1988).
24. Dan, J., Geirnaert, S. & Bertrand, A. Grouped variable selection for generalized eigenvalue problems. *Signal Processing* **195** (2022).
25. Harid, N. M. *et al.* Measuring expertise in identifying interictal epileptiform discharges. *Epileptic Disorders* **24,** 496–506 (3 2022).
26. Kural, M. A. *et al.* Criteria for defining interictal epileptiform discharges in EEG. *Neurology* **94,** e2139–e2147 (20 2020).
27. Jing, J. *et al.* Interrater Reliability of Experts in Identifying Interictal Epileptiform Discharges in Electroencephalograms. *JAMA neurology* **77,** 49–57 (1 2020).
28. Reus, E., Cox, F., van Dijk, J. & Visser, G. Automated spike detection: Which software package? *Seizure* **95,** 33–37 (2022).
29. Bushby, K. M., Cole, T., Matthews, J. N. & Goodship, J. A. Centiles for adult head circumference. *Archives of Disease in Childhood* **67,** 1286–1287 (10 1992).
30. Brummelen, G. V. *Heavenly mathematics: The forgotten art of spherical trigonometry* (Princeton University Press, 2012).
31. Wouters, J., Kloosterman, F. & Bertrand, A. A data-driven regularization approach for template matching in spike sorting with high-density neural probes. *Annual International Conference of the IEEE Engineering in Medicine and Biology Society.* **2019,** 4376–4379 (2019).
32. Steinarsson, S. *Downsampling Time Series for Visual Representation* (University of Iceland, 2013).
33. Basu, S., Banerjee, M. & Sen, A. Bayesian Inference for Kappa from Single and Multiple Studies. *Biometrics* **56,** 577–582 (2 2000).
34. Ferrari, S. & Cribari-Neto, F. Beta Regression for Modelling Rates and Proportions. *Journal of Applied Statistics* **31,** 799–815 (7 2004).
35. Kruschke, J. K. Bayesian estimation supersedes the t test. *Journal of experimental psychology* **142,** 573–603 (2 2013).
36. Salvatier, J., Wiecki, T. V. & Fonnesbeck, C. Probabilistic programming in Python using PyMC3. *PeerJ Computer Science* **2016,** e55 (4 2016).
37. Halford, J. J., Sabau, D., Drislane, F. W., Tsuchida, T. N. & Sinha, S. R. American Clinical Neurophysiology Society Guideline 4: Recording Clinical EEG on Digital Media. *Journal of clinical neurophysiology* **33,** 317–319 (4 2016).
38. *ADS1299-x Low-Noise, 4-, 6-, 8-Channel, 24-Bit, Analog-to-Digital Converter for EEG and Biopotential Measurements datasheet* ADS1299. Rev. C. Texas Instruments (2017). `https://www.ti.com/lit/gpn/ads1299`.
39. Bleichner, M. G. *et al.* Exploring miniaturized EEG electrodes for brain-computer interfaces. An EEG you do not see? *Physiological reports* **3** (4 2015).